

Comparative analysis of structural, elastic, electronic, phonon, thermal and optical properties of two $\text{Na}_6\text{Ge}_2\text{Se}_6$ phases from first principles calculations

Qi Zhang and Aleksandr Chernatynskiy

Department of Physics, Missouri University of Science and Technology, Missouri, Rolla 65401, USA

Amitava Choudhury

Department of Chemistry, Missouri University of Science and Technology, Missouri, Rolla 65401, USA

The demand for new alkali metal chalcogenide materials is continuously increasing due to their potential applications across various technological fields. Recently, a new compound, $\text{Na}_6\text{Ge}_2\text{Se}_6$, was computationally predicted, representing a new phase distinct from the experimentally observed $\text{Na}_6\text{Ge}_2\text{Se}_6$ reported in 1985. Notably, this newly predicted phase displays a lower total energy compared to the previously known experimental phase, as determined by first-principles calculations. In this study, we undertake a thorough comparative analysis of the structural, elastic, electronic, phonon, thermal, and optical properties of these two $\text{Na}_6\text{Ge}_2\text{Se}_6$ phases. Our results show that both phases meet mechanical and dynamical stability criteria. The electronic band structure analysis confirms the semiconducting nature of both materials, with a 2.97 eV indirect band gap for the predicted phase and a 2.93 eV direct band gap for the observed phase. Optically, both phases exhibit strong absorption in the ultraviolet region. Thermal properties analysis reveals that the predicted phase is more thermodynamically stable below 907 K, while the observed phase shows greater thermodynamic stability above this temperature.

INTRODUCTION

Ternary alkali metal-based chalcogenides are characterized by the general formula ABZ where A signifies an alkali metal (Li, Na, K), B includes main group elements (e.g., Ge, Bi) or transition metals (e.g., Fe, Cu), while Z represents chalcogen elements (e.g., S, Se). These compounds have gained considerable interest recently for their potential applications in energy conversion/storage, optoelectronics, and thermoelectrics. These areas are vital for supporting the advancement of current technologies and industries, especially in addressing the global energy challenge as society aims to transition from fossil fuels to renewable, efficient, and eco-friendly energy solutions. In response to these demands, numerous ABZ compounds have been synthesized and explored.

In the quest for improved energy storage solutions, the focus on ion-battery anodes is crucial due to their significant impact on battery performance. ABZ materials like LiLnSe_2 and NaFeS_2 have shown high storage capacities and efficient energy cycling in recent studies [1, 2], with NaFeS_2 showcasing excellent cycling stability as a Li-ion battery anode, suggesting potential for enhanced battery lifespan and reliability. Optoelectronically, ABZ compounds such as NaSbS_2 offer strong absorption in the visible spectrum, and their affordability, abundance, and non-toxicity make them attractive for solar energy applications[3]. Furthermore, in thermoelectric applications, ABZ materials like CsAg_5Te_3 exhibit promising mid-temperature performance with high ZT values[4], thanks to their intrinsically low thermal conductivity[5–7]. Ternary chalcogenides have also played a crucial role in enabling the synthesis of more complex multi-ary chalcogenides in a rational manner[8]. Many of

these compounds have demonstrated significant technological potential. For instance, outstanding electric thermal properties have been observed in materials like $\text{Na}_{0.95}\text{Pb}_{19}\text{SbTe}_{22}$, achieving a ZT value greater than 1 across one of the broadest temperature ranges (475 to 650 K) reported for any single material[9]. Additionally, a study on $\text{Na}_{1-x}\text{K}_x\text{AsQ}_2$ ($Q = \text{S, Se}$) highlighted its potential applications in signal processing and data transmission, attributed to its nonlinear optical properties[10].

Although many ABZ compounds have been synthesised, the existing collection of these ternary ABZ compounds still lacks many possible combinations. The process of discovering new materials through purely experimental means is often prolonged, as the growth and characterization of their properties can be time-consuming. With the increase of computational power, simulations are increasingly employed in material discovery, for both screening of the properties of already known materials as well as prediction of the new compounds. Recently, a new structure of the chalcogenide, $\text{Na}_6\text{Ge}_2\text{Se}_6$ was computationally predicted using simulated annealing and first-principles methods[11]. This compound represents a new phase distinct from the experimentally observed compound reported in 1985 with the same composition ($\text{Na}_6\text{Ge}_2\text{Se}_6$)[12]. The latter has been utilized recently in synthesizing a potential nonlinear optical material, $\text{Na}_8\text{Mn}_2(\text{Ge}_2\text{Se}_6)_2$ [8]. Notably, the newly predicted $\text{Na}_6\text{Ge}_2\text{Se}_6$ phase shows a lower total energy compared to the observed phase from first-principles calculations, suggesting it as a potential meta-stable state of $\text{Na}_6\text{Ge}_2\text{Se}_6$ that has not been reported before. Furthermore, the observed $\text{Na}_6\text{Ge}_2\text{Se}_6$ phase has received little attention, with no comprehensive analysis conducted to the best of our knowledge. This gap in research has motivated us

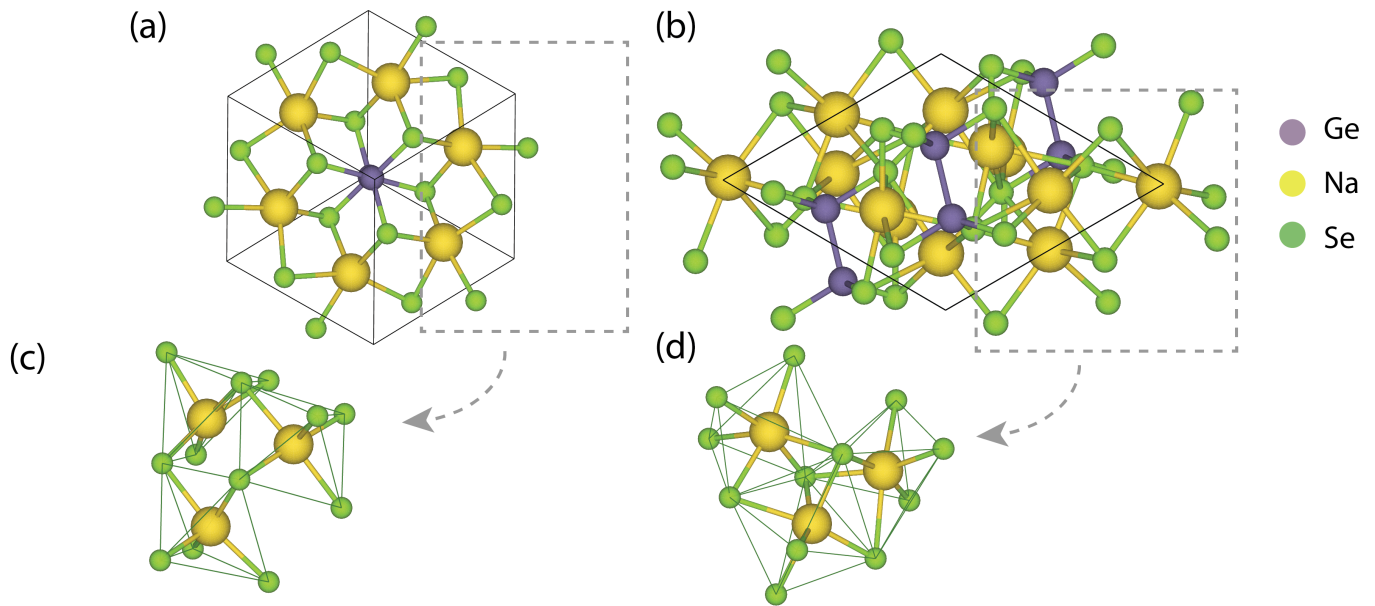


FIG. 1: Crystal structures of both Na₆Ge₂Se₆ phases. (a) Predicted new Na₆Ge₂Se₆ phase. (b) Observed Na₆Ge₂Se₆ phase. (c) One Na atom and five Se atoms form a [NaSe₅] pyramid. (d) One Na atom and six Se atoms form a [NaSe₆] distorted octahedron.

to perform a comparative analysis of the structural, elastic, electronic, phonon, thermal, and optical properties of these two compounds, which could serve as a valuable reference for future studies.

COMPUTATIONAL METHODOLOGY

In this study, we examined the ground state properties of both predicted and observed Na₆Ge₂Se₆ phases using density functional theory (DFT) as implemented in the Vienna Ab initio Simulation Package (VASP)[13, 14]. This involved solving the Kohn-Sham equations[15] to determine the ground state energies of a crystalline system. Given the close proximity of the ground state energies between the predicted and observed phases, calculations were performed using two distinct approaches for the exchange-correlation potential: the Generalized Gradient Approximation (GGA) within the Perdew-Burke-Ernzerhof framework (GGA-PBE)[16] and the hybrid functionals from Heyd-Scuseria-Ernzerhof (HSE06)[17]. In both Na₆Ge₂Se₆ structures, Integration over the Brillouin zone was executed via the tetrahedron method with Gaussian smearing, employing a $5 \times 5 \times 5$ Monkhorst-Pack k-point mesh[18]. The energy cutoff for the plane wave basis set was set to 600 eV. The Ge $3d^{10}4s^34p^2$, Se $4s^2p^4$, Na $2p^63s^1$ electrons are treated as valence electrons. convergence thresholds were 1×10^{-8} eV for the electronic self-consistent loop and 1×10^{-7} eV for structure optimization.

Further, we explored the elastic and dynamical prop-

erties of optimized structures using first-principle calculations with the GGA-PBE functional within VASP. This analysis allowed for the calculation of elastic constants C_{ij} and several elastic properties, including the bulk modulus B , Young's modulus E and shear modulus G , along with optical properties such as the dielectric function $\epsilon(\omega)$, absorption coefficient $\alpha(\omega)$ and conductivity $\sigma(\omega)$ using the VASPKIT[19] tool. The Phonopy package[20, 21] facilitated the calculation of phonon dispersion relations, phonon density of states, and related thermal properties. Considering the tendency of GGA-PBE to underestimate band gaps in semiconductors and insulators, the HSE06 functional[17] was applied to investigate electronic and optical properties. The electronic band structures and density of states for both phases were visualized using the open-source Python library Pymatgen[22].

CRYSTAL STRUCTURE

We analyzed the Na₆Ge₂Se₆ structures using two different exchange-correlation energy functionals: GGA-PBE and the HSE06 hybrid functional. The calculated energies per atom are presented in Table I. Both PBE and HSE06 functionals indicated lower energies for the predicted Na₆Ge₂Se₆ phase by 16 meV/atom. To confirm the convergence of our DFT calculations, we conducted two additional structure relaxations with the GGA-PBE functional: one with a 400 eV energy cutoff and a $3 \times 3 \times 3$ k-point mesh, and another with a 500 eV energy cutoff

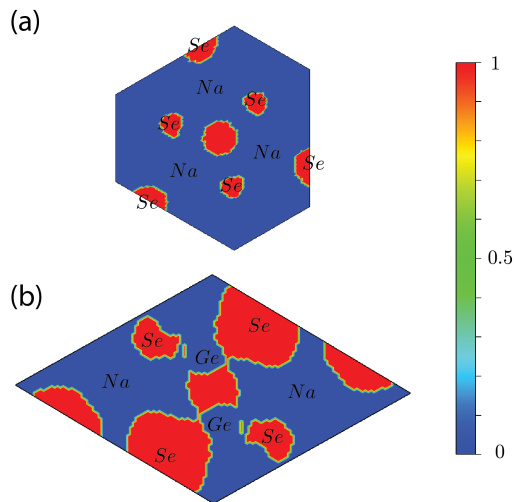


FIG. 2: Electron localization function (ELF) (a) Predicted $\text{Na}_6\text{Ge}_2\text{Se}_6$ phase. (b) Observed $\text{Na}_6\text{Ge}_2\text{Se}_6$ phase.

and a $4 \times 4 \times 4$ k-point mesh. For the predicted phase, both of these settings produced energy per atom within 0.006% of the most accurate result listed in the Table I. For the observed phase, the difference is even smaller, within 0.002%. The energy difference between the predicted and observed phases listed above is an order of magnitude larger than 0.06%, thus numerical accuracy is sufficient to make conclusions about the energy order of two structures. This leads us to conclude that the predicted $\text{Na}_6\text{Ge}_2\text{Se}_6$ phase is energetically more favorable than the observed one at 0 K.

The predicted $\text{Na}_6\text{Ge}_2\text{Se}_6$ crystallizes in the space group $R\bar{3}$ (No.148), whereas the observed phase is found in the space group $P2_1/c$ (No.14). Both structures exhibit identical ethane-like selenide $[\text{Ge}_2\text{Se}_6]$ units, featuring a Ge-Ge bond length of 2.49 Å for the predicted phase and 2.47 Å for the observed phase, and an average Ge-Se bond length of 2.39 Å as detailed in Table II. These bond lengths are slightly greater than the originally observed $\text{Na}_6\text{Ge}_2\text{Se}_6$ data[12], which recorded a Ge-Ge bond length of 2.43 Å and a Ge-Se bond length of 2.33 Å. The $[\text{Ge}_2\text{Se}_6]$ ethane-like dimer configuration bears similarity to the $[\text{P}_2\text{Se}_6]$ in $\text{Mg}_2\text{P}_2\text{Se}_6$ [23], and $[\text{Si}_2\text{Se}_6]$ in $\text{Na}_4\text{MgSi}_2\text{Se}_6$ [24]. For both $\text{Na}_6\text{Ge}_2\text{Se}_6$ phases, the formed $[\text{Ge}_2\text{Se}_6]$ dimers are isolated from each other, similar to the cases in $\text{K}_6\text{Ge}_2\text{Se}_6$ [25] and $\text{Cs}_6\text{Ge}_2\text{Se}_6$ [26]. The predicted $\text{Na}_6\text{Ge}_2\text{Se}_6$ phase exhibits cell parameters of $a = 11.349$ Å, $b = 11.349$ Å, $c = 10.900$ Å, $\alpha = 90^\circ$, $\beta = 90^\circ$ and $\gamma = 120^\circ$, while the observed $\text{Na}_6\text{Ge}_2\text{Se}_6$ has $a = 8.445$ Å, $b = 12.038$ Å, $c = 8.316$ Å, $\alpha = 90^\circ$, $\beta = 118.877^\circ$ and $\gamma = 90^\circ$ with a smaller unit cell volume. The predicted $\text{Na}_6\text{Ge}_2\text{Se}_6$ features only one crystallographically unique Na atom, one Ge atom, and one Se

TABLE I: : Crystal data and DFT evaluated energy of predicted and observed $\text{Na}_6\text{Ge}_2\text{Se}_6$

	Predicted	Observed
Empirical formula	$\text{Na}_6\text{Ge}_2\text{Se}_6$	$\text{Na}_6\text{Ge}_2\text{Se}_6$
Crystal system	Trigonal	Monoclinic
Space group	$R\bar{3}$	$P2_1/c$
Unit cell	$a = 11.349$ Å	$a = 8.445$ Å
	$b = 11.349$ Å	$b = 12.038$ Å
	$c = 10.900$ Å	$c = 8.316$ Å
	$\alpha = 90^\circ$	$\alpha = 90^\circ$
	$\beta = 90^\circ$	$\beta = 118.877^\circ$
	$\gamma = 120^\circ$	$\gamma = 90^\circ$
Volume (Å ³)	$V = 405.27$	740.20
Z	1	2
Density(ρ)	3.075 g/cm ⁻³	3.367 g/cm ⁻³
Energy (eV/atom)		
GGA-PBE	-3.598	-3.582
HSE06	-4.268	-4.252

TABLE II: : Bond distance within the $[\text{Ge}_2\text{Se}_6]$ block for predicted and observed $\text{Na}_6\text{Ge}_2\text{Se}_6$

	Predicted	Observed
Ge-Ge	2.49 Å	Ge-Ge 2.47 Å
Ge-Se	2.39 Å	Ge-Se 2.38 Å

atom, contrasting with the observed $\text{Na}_6\text{Ge}_2\text{Se}_6$, which has three unique Na atoms, one Ge atom, and three Se atoms. In the predicted $\text{Na}_6\text{Ge}_2\text{Se}_6$, each Na atom coordinates with five Se atoms to form a $[\text{NaSe}_5]$ pyramid. This pyramid shares corners with its neighboring $[\text{NaSe}_5]$ pyramids, whereas in the observed phase, each Na atom bonds with six Se atoms to form a $[\text{NaSe}_6]$ slightly distorted octahedron. These octahedra are connected by face-sharing with their neighboring $[\text{NaSe}_6]$ octahedron, as illustrated in Fig. 1(c) and Fig. 1(d). The electron localization function (ELF) provides a visual representation of valence electron distribution[27], highlighting features that correspond to chemical bonding characteristics. Fig. 2 shows that areas near the center of Se atoms and between Ge/Ge atoms exhibit ELF values close to 1.

ELASTIC PROPERTIES

Analyzing the elastic properties offers insights into the mechanical behavior of compounds, including their stability, ductility, and brittleness. Such information is especially valuable in industrial and device manufacturing sectors, enhancing our understanding of the forces acting in solids. To calculate elastic constants, we employed the energy-strain method[28], as facilitated by VASP[19] based on DFT calculations with GGA-PBE functional.

For the predicted $\text{Na}_6\text{Ge}_2\text{Se}_6$ phase, which crystallizes

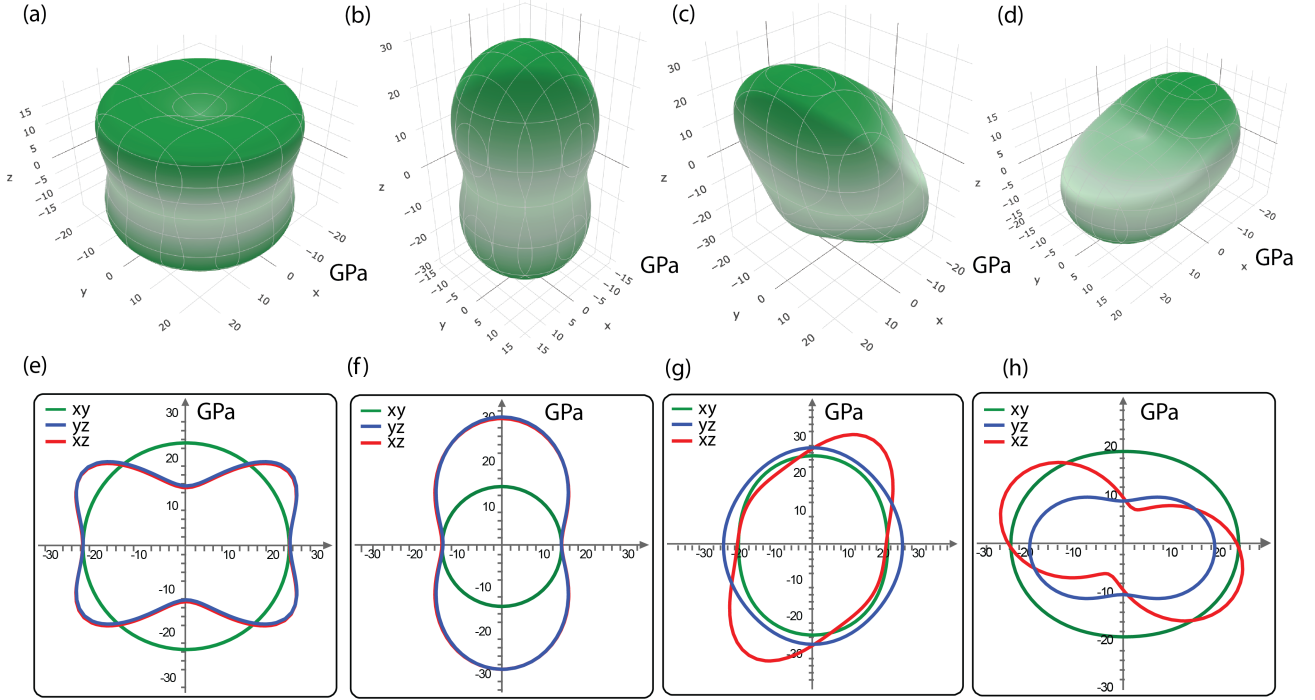


FIG. 3: 3D representations of the spatial dependence of the Young's modulus and linear compressibility for (a) and (b) the predicted $\text{Na}_6\text{Ge}_2\text{Se}_6$ phase, and (c) and (d) the observed $\text{Na}_6\text{Ge}_2\text{Se}_6$ phase. Their cross-sections in the x-, y-, and z-directions are shown below.

in the trigonal crystal system, There are five independent elastic constants: C_{11} , C_{33} , C_{44} , C_{12} , C_{13} with the added relation

$$C_{66} = (C_{11} - C_{12})/2 \quad (1)$$

This contrasts with its observed counterpart, which crystallizes in monoclinic crystal system with lower symmetry that has thirteen independent elastic constants: C_{11} , C_{12} , C_{13} , C_{15} , C_{22} , C_{23} , C_{25} , C_{33} , C_{35} , C_{44} , C_{46} , C_{55} and C_{66} . The configurations of these constants constitute the elastic matrices for each respective phase as follows:

$$C_{\text{predicted}} = \begin{pmatrix} 32.06 & 10.86 & 13.31 & \cdot & \cdot & \cdot \\ \cdot & 32.06 & 13.31 & \cdot & \cdot & \cdot \\ \cdot & \cdot & 21.06 & \cdot & \cdot & \cdot \\ \cdot & \cdot & \cdot & 12.09 & \cdot & \cdot \\ \cdot & \cdot & \cdot & \cdot & 12.09 & \cdot \\ \cdot & \cdot & \cdot & \cdot & \cdot & 10.60 \end{pmatrix}$$

$$C_{\text{observed}} = \begin{pmatrix} 28.28 & 10.82 & 15.82 & \cdot & 2.45 & \cdot \\ \cdot & 32.08 & 15.21 & \cdot & 1.55 & \cdot \\ \cdot & \cdot & 40.55 & \cdot & 4.76 & \cdot \\ \cdot & \cdot & \cdot & 10.43 & \cdot & 2.81 \\ \cdot & \cdot & \cdot & \cdot & 10.67 & \cdot \\ \cdot & \cdot & \cdot & \cdot & \cdot & 10.75 \end{pmatrix}$$

These elastic constants are pivotal for assessing other elastic properties. A crystal must satisfy the Born-Huang

TABLE III: : Calculated mechanical properties of polycrystal for both predicted and observed $\text{Na}_6\text{Ge}_2\text{Se}_6$ (all in GPa)

	B	E	G	ν	B/G	ζ
Predicted	17.543	24.407	9.623	0.268	1.82	0.59
Observed	19.770	25.731	10.027	0.283	1.97	0.65

criteria[29] to be deemed mechanically stable. For the predicted structure, the necessary and sufficient Born-Huang criteria include:

$$C_{11} > |C_{12}|, C_{44} > 0, C_{66} > 0 \quad (2)$$

$$2C_{13}^2 < C_{33}(C_{11} + C_{12}) \quad (3)$$

Due to the intricacy of these criteria for the monoclinic system, their detailed equations are not listed here. Crucially, the calculated elastic constants for both $\text{Na}_6\text{Ge}_2\text{Se}_6$ phases fulfill their respective stability criteria, indicating mechanical stability for both the predicted and observed phases.

Constants C_{11} , C_{22} and C_{33} quantify the response to uniaxial strain along the three principal axes. The differences between these constants measure the extent of anisotropy in linear compressibility. From matrix $C_{\text{predicted}}$ and C_{observed} , we can see that for predicted

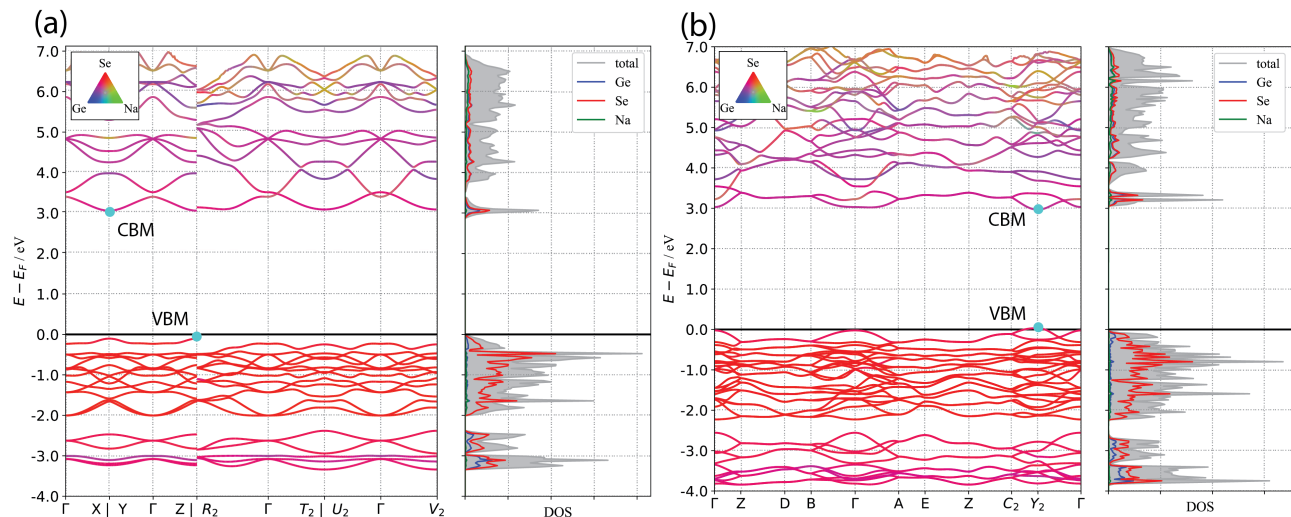


FIG. 4: Electronic band structures (BS) and density of states (DOS) of both $\text{Na}_6\text{Ge}_2\text{Se}_6$ compounds. (a) BS and DOS for predicted $\text{Na}_6\text{Ge}_2\text{Se}_6$ phase. (b) BS and PDOS for observed $\text{Na}_6\text{Ge}_2\text{Se}_6$ phase

phase, $C_{11} = C_{22} > C_{33}$ which means linear compressibility is isotropic in the x- and y-directions and greater than in the z-direction. For the observed phase, $C_{33} > C_{22} > C_{11}$, indicating that the observed $\text{Na}_6\text{Ge}_2\text{Se}_6$ phase is characterized by anisotropic linear compressibility. While both phases have similar resistance to deformation along the x- and y-directions, the observed phase is significantly stiffer in the z-direction.

On the other hand, C_{44} , C_{55} and C_{66} assess the material's resistance to shear deformation about these axes. The elastic constant matrix for the predicted $\text{Na}_6\text{Ge}_2\text{Se}_6$ phase exhibits $C_{44} = C_{55}$ and slightly smaller C_{66} , indicating its shear modulus is weakly anisotropic. For this phase, the resistance to shear deformation is isotropic about the x- and y-directions and greater than that in the z-direction. Comparing both phases, the observed phase shows slightly higher resistance to shear deformation about the principal axes.

The off-diagonal terms indicate coupling between different deformation modes. For instance, C_{12} correlates the stress applied in the x-direction to the resultant strain in the y-direction. Analysis of the matrices suggests that both phases have a similar response to deformation in the y-direction when stress is applied in the x-direction. However, the predicted phase shows greater shear strain in the z-direction induced by stress in both the x- and y-directions.

Utilizing the independent elastic constants, we can derive key mechanical properties such as the bulk modulus (B), shear modulus (G), Young's modulus (E), and Poisson's ratio (ν) through the following relations, with the calculated values presented in Table III:

$$B = \frac{B_V + B_R}{2} \quad (4)$$

$$G = \frac{G_V + G_R}{2} \quad (5)$$

$$E = \frac{9BG}{3B + G} \quad (6)$$

$$\nu = \frac{3B - 2G}{2(3B + G)} \quad (7)$$

Here, B_V , B_R and G_V , G_R represent the Voigt[30] and Reuss[31] values of the bulk modulus and shear modulus respectively. Furthermore, we evaluated Kleinman's parameter (ζ) using VASPKIT[19].

The bulk and shear moduli offer insights into a crystal's mechanical behavior, indicating its resistance to volumetric and shape deformations, respectively. The data in the Table III reveal that the observed $\text{Na}_6\text{Ge}_2\text{Se}_6$ phase possesses a greater resistance to deformation. This is expected as the unit-cell volume of the predicted phase is greater than that of the observed phase. Pugh's ratio (B/G) serves as a gauge for a material's ductility or brittleness, with a threshold value of 1.75 distinguishing between the two behaviors where the material is claimed to be brittle, if $B/G < 1.75$ and classified to be ductile if $B/G > 1.75$ [32]. Our findings suggest that both phases exhibit ductility. The stiffness and thermal shock resistance of these materials are inferred from Young's modulus (E)[33], indicating superior stiffness in the observed phase. Conversely, a lower Young's modulus hints at enhanced thermal shock resistance[34] for the predicted phase. Poisson's ratio (ν) sheds light on the nature of bonding forces within a crystal and aids in evaluating its mechanical properties, including stability against shear[35]. Values for the predicted and observed phases

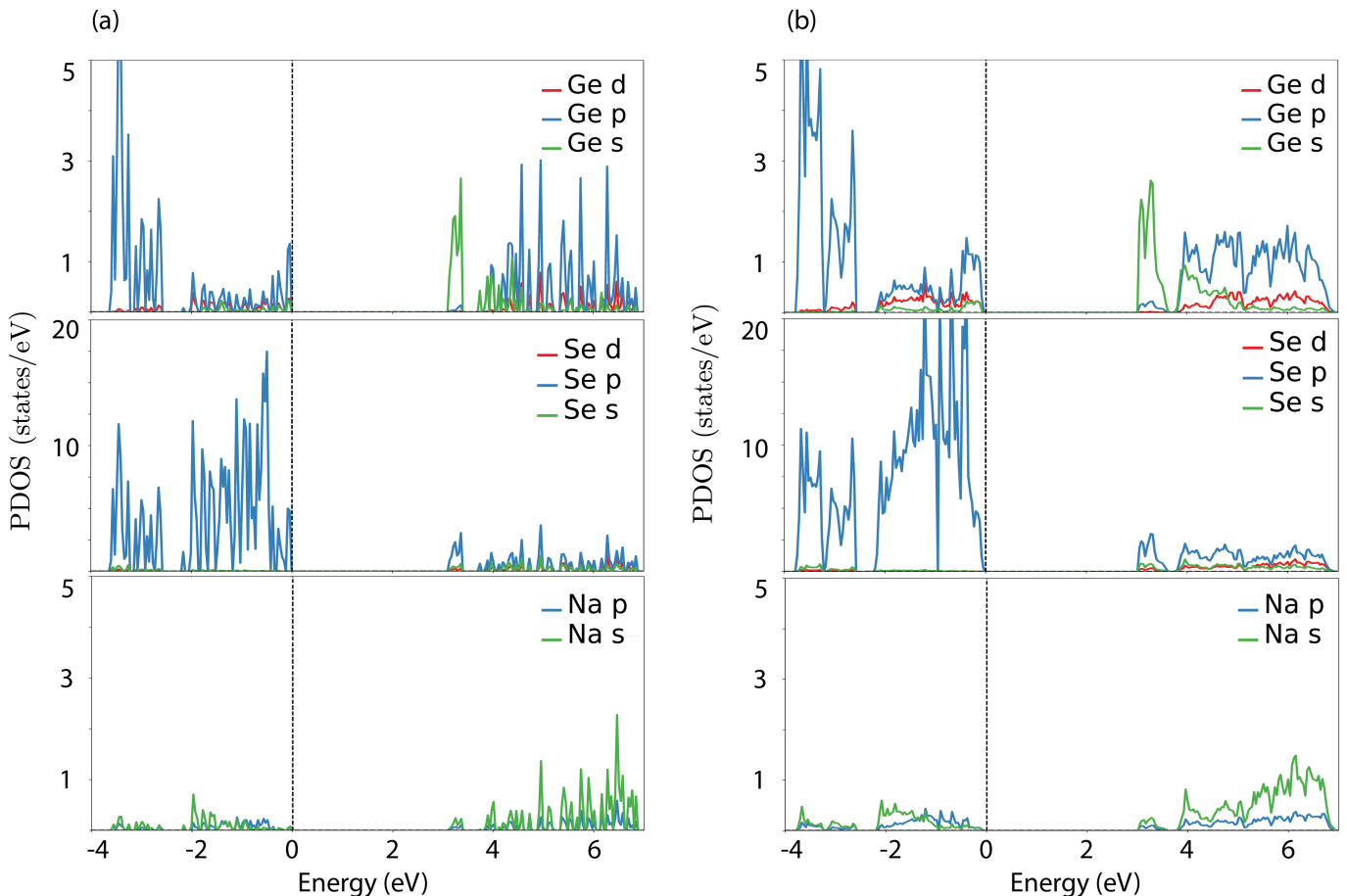


FIG. 5: The partial density of states (PDOS) on orbitals and elements for (a) the predicted $\text{Na}_6\text{Ge}_2\text{Se}_6$ and (b) the observed $\text{Na}_6\text{Ge}_2\text{Se}_6$.

are 0.268 and 0.283, respectively, falling within the central force solids' expected range of 0.25 to 0.50[36]. This metric also predicts the material's ductility or brittleness, classifying those with $\nu > 0.26$ as ductile and those below 0.26 as brittle[34, 37]. Thus, our analysis corroborates both phases' ductility, aligning with conclusions drawn from Pugh's ratio. Lastly, the Kleinman parameter (ζ), varying between 0 and 1, indicates the dominance of bond stretching or bending in resisting external stress[38] where the lower value of the Kleinman parameter ζ indicates a minimal role of bond bending in resisting external stress, whereas a higher value suggests a negligible contribution of bond stretching or contracting to resist externally applied stress. For both $\text{Na}_6\text{Ge}_2\text{Se}_6$ phases, a $\zeta > 0.5$ indicates a major role for bond bending in its mechanical strength.

Fig. 3 shows the 3D and 2D representations of Young's modulus and linear compressibility for both $\text{Na}_6\text{Ge}_2\text{Se}_6$ phases. For the predicted phase, the Young's modulus and linear compressibility in the xy-plane form a circle, as shown in Figures 3(e) and (f), suggesting both properties are isotropic within the xy-plane. However, both proper-

ties show significant deviation from a circular form within the yz- and xz-planes, indicating that Young's modulus and linear compressibility are anisotropic overall for the predicted $\text{Na}_6\text{Ge}_2\text{Se}_6$. For the observed phase, Figures 3(g) and (h) show that both properties are anisotropic, with the 2D representation of Young's modulus in the xy- and yz-planes and linear compressibility in the xy-plane more closely resembling a circle. This suggests relative isotropy for both properties within the corresponding planes.

ELECTRONIC PROPERTIES

We present the electronic band structure along with the partial and total density of states (DOS) in Fig. 4. These calculations were performed using optimized lattice parameters along high-symmetry directions in the first Brillouin zone. The partial density of states (PDOS) on orbitals and elements are depicted in Fig. 5. The band structures and DOS for both $\text{Na}_6\text{Ge}_2\text{Se}_6$ phases were determined using the HSE06 hybrid exchange-correlation

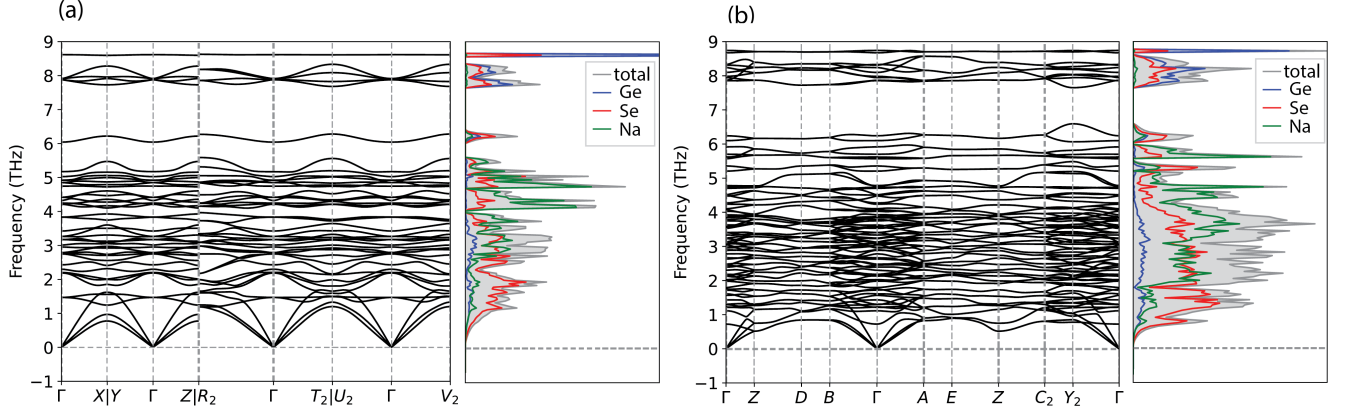


FIG. 6: Phonon density of states and band structure of both $\text{Na}_6\text{Ge}_2\text{Se}_6$ compounds. (a) Predicted new $\text{Na}_6\text{Ge}_2\text{Se}_6$ phase. (b) Observed $\text{Na}_6\text{Ge}_2\text{Se}_6$ phase.

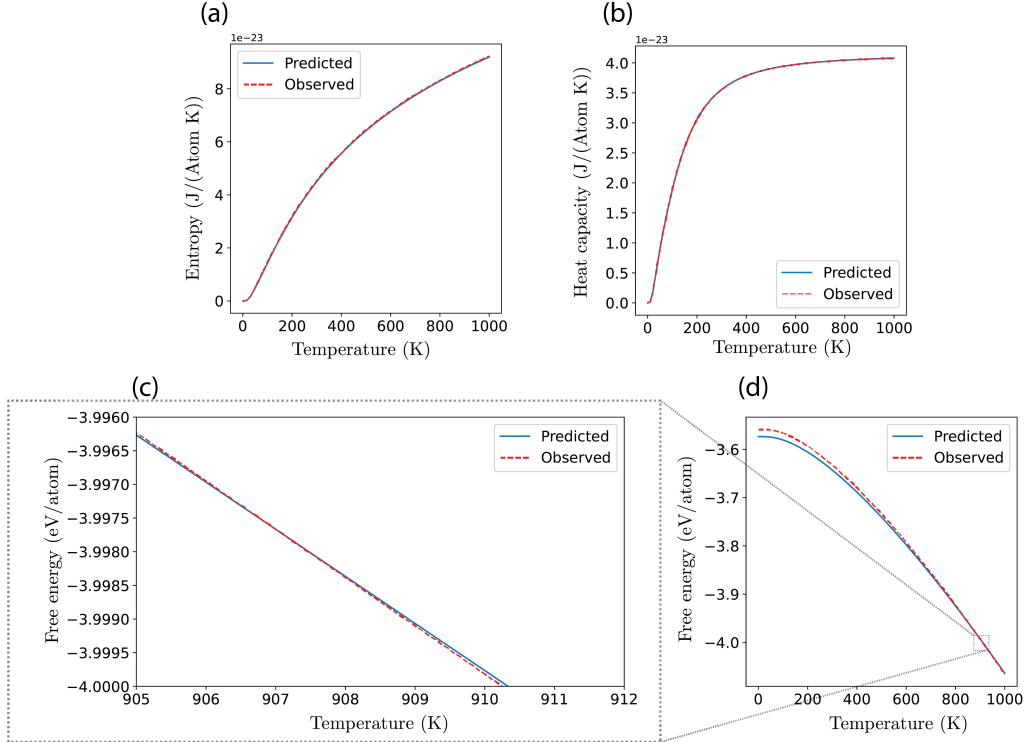


FIG. 7: Thermal properties comparison between predicted and observed $\text{Na}_6\text{Ge}_2\text{Se}_6$ phases. (a) Entropy. (b) Heat capacity. (c) Helmholtz free energy in the temperature range from 905K to 912K. (d) Helmholtz free energy in the temperature range from 0K to 1000K

functional[17] to ensure enhanced accuracy[39]. The energy reference point is set at the top of the valence band. The band structure analysis reveals that the predicted $\text{Na}_6\text{Ge}_2\text{Se}_6$ phase possesses an indirect band gap, with the conduction band minimum (CBM) located at the X -point and the valence band maximum (VBM) at the Z -point, resulting in a band gap of 2.972 eV. In contrast,

the observed $\text{Na}_6\text{Ge}_2\text{Se}_6$ phase exhibits a direct band gap of 2.932 eV, with both the CBM and VBM situated at the Y_2 -point.

From Fig. 5, we observe that both phases share similar orbital and element contributions to the total DOS. Regions close to the Fermi level are predominantly influenced by contributions from Se-p and Ge-s orbitals,

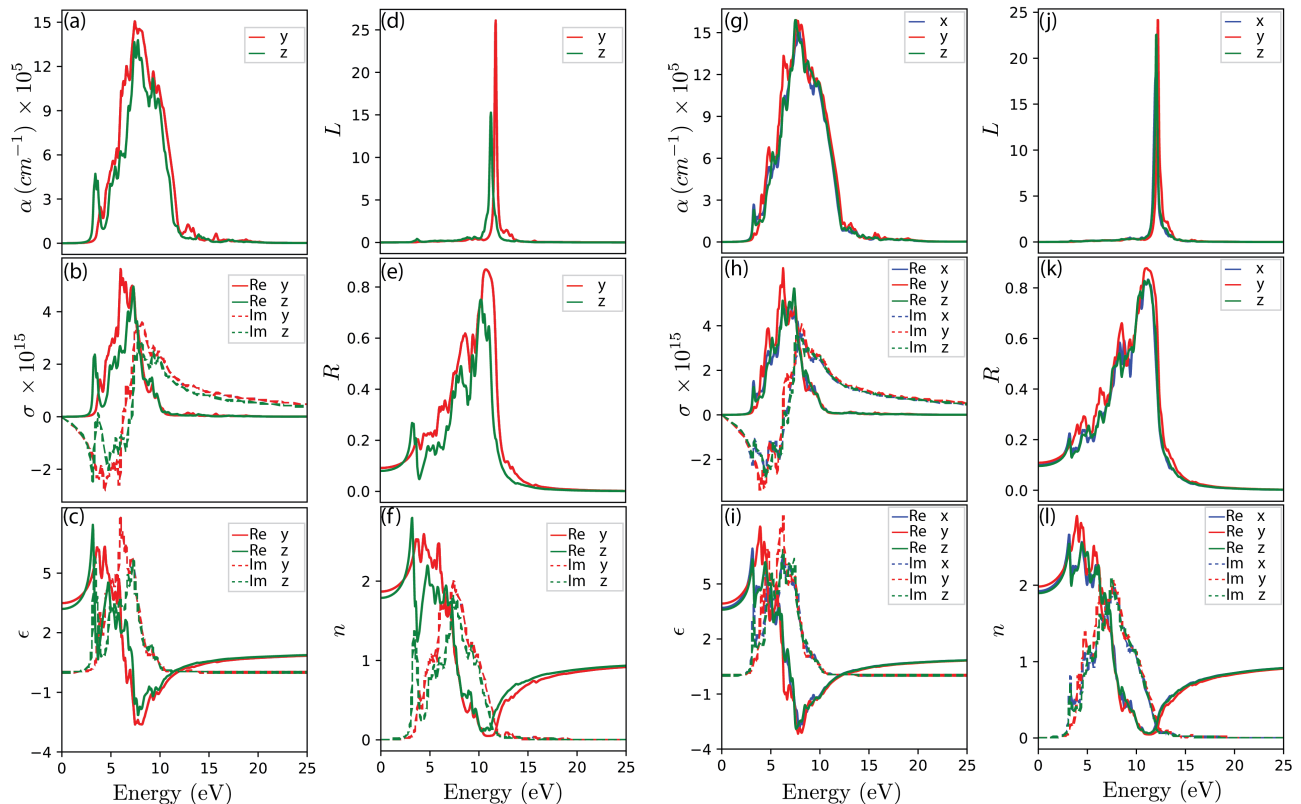


FIG. 8: (a)(b)(c)(d)(e)(f) are the optical properties for predicted $\text{Na}_6\text{Ge}_2\text{Se}_6$, (g)(h)(i)(j)(k)(l) are the optical properties for observed $\text{Na}_6\text{Ge}_2\text{Se}_6$. (a)(g): Absorption coefficient α , (b)(h): Conductivity σ , (c)(i): Dielectric function ϵ , (d)(j): Energy-loss function L , (e)(k): Reflectivity R , (f)(l): Refractive index n .

while Na's involvement near the Fermi level is minimal. This observation suggests that the band gaps in both $\text{Na}_6\text{Ge}_2\text{Se}_6$ phases are largely attributable to the $[\text{Ge}_2\text{Se}_6]$ dimers. Within the valence band, ranging from -4 to 0 eV, the primary contributions come from Se-p and Ge-p orbitals in both phases. This trend extends to the lower regions of the conduction band, from 4 to 8 eV, where Na-p displays a slight contribution to the total DOS in this region.

PHONON AND THERMAL PROPERTIES

Investigating phonon properties is fundamental for understanding crystalline materials, as it provides insights into structural stability, phase transitions, and how vibrations influence their thermal behavior. In our study of the phonon dispersion and phonon band structures for both $\text{Na}_6\text{Ge}_2\text{Se}_6$ phases, we employed the Phonopy package[20, 21] to create a series of $2 \times 2 \times 2$ supercell structures with various displacements. We then conducted force calculations using VASP, employing the GGA-PBE exchange-correlation functional. The phonon frequencies and eigenvectors were determined from the

dynamical matrices, which were calculated based on the force constants derived using Phonopy.

The phonon dispersion relations along high-symmetry paths for both phases are depicted in Fig. 6. The unit cell of the predicted phase comprises 14 atoms, resulting in 42 phonon branches, while the observed phase has 28 atoms, resulting in 82 branches, which include three acoustic and the rest optical branches. The frequency spectrum of these modes spans from 0 to 10 THz, without any discernible gap between the acoustic and optical modes for either phase. In the lower frequency domain, below 7 THz, Na and Se atoms predominantly contribute to the optical branches. In the higher frequency range, the contributions mainly stem from Ge and Se. This distribution underscores the strong bonding present within the $[\text{Ge}_2\text{Se}_6]$ dimers, reflecting their structural integrity across both phases of $\text{Na}_6\text{Ge}_2\text{Se}_6$. The lack of negative frequency branches within the dispersion plots affirms the dynamic stability of these phases at zero pressure.

The Debye temperature (θ_D) represents the temperature corresponding to the highest energy vibrational

TABLE IV: : Calculated v_t , v_l , v_m and θ_D for both predicted and observed $\text{Na}_6\text{Ge}_2\text{Se}_6$

	v_t (m/s)	v_l (m/s)	v_m (m/s)	θ_D (K)
Predicted	1761.41	3129.30	1959.71	190.0
Observed	1725.51	3136.88	1923.28	191.7

mode in a solid, derived from the equation[40]:

$$\theta_D = \frac{h}{k_B} \left[\frac{3n}{4\pi V_0} \right]^{\frac{1}{3}} v_m \quad (8)$$

Here, h is the Planck's constant, k_B is the Boltzmann's constant, n is the number of atoms in the unit cell, V_0 is the unit cell's equilibrium volume, and v_m is the material's average speed of sound. The average speed of sound v_m can be determined from the material's mass density (ρ), along with its bulk (B) and shear modulus (G), through the equations for longitudinal (v_l) and transverse (v_t) sound speeds:

$$v_m = \left[\frac{1}{3} \left(\frac{3}{v_t^3} + \frac{1}{v_l^3} \right) \right]^{\frac{1}{3}} \quad (9)$$

$$v_t = \sqrt{\frac{G}{\rho}} \quad (10)$$

$$v_l = \sqrt{\frac{3B + 4G}{3\rho}} \quad (11)$$

The calculated values for v_t , v_l , v_m and θ_D are provided in Table IV. These values indicate that the predicted $\text{Na}_6\text{Ge}_2\text{Se}_6$ phase exhibits a slower longitudinal speed of sound but a higher transverse one than observed phase, although the values differ only slightly. The Debye temperature of the predicted phase is approximately 0.89% lower than that of its counterpart.

Phonon calculations offer insights into additional thermal properties such as entropy (S), constant-volume heat capacity (C_v), and Helmholtz free energy (F), which are depicted in Fig. 7. The heat capacity curves, as one can see from Fig. 7(b), are almost indistinguishable as one expects from similar speeds of sound and Debye temperatures. They show standard Debye theory behavior with the increasing temperature: quantum T^3 at low temperature, saturating to the constant classical Dulong-Petit limit[41] above Debye temperature.

The calculation of the Helmholtz free energy (F) within the harmonic approximation[42] facilitates an evaluation of the thermal contributions to the relative stability of two phases, as described by the following

equation:

$$F = E_{total} + \frac{1}{2} \sum_{q\nu} \hbar\omega(q\nu) + k_B T \sum_{q\nu} \ln [1 - \exp(-\hbar\omega(q\nu)/k_B T)] \quad (12)$$

Here, E_{total} denotes the total energy of the crystal, available in Table I. The summed terms represent the Helmholtz free energy attributable to phonons[43], with the initial sum reflecting the zero-point energy (ZPE) that is independent of temperature. The predicted phase's ZPE is approximately 1 meV/atom higher than that of the observed phase. The subsequent sum accounts for the temperature-dependent term referring to the thermally induced occupation of phonon modes. The Helmholtz free energies, plotted in Fig. 7(d) for temperatures ranging from 0 to 1000 K, with a closer look at the range of 905 to 912 K in Fig. 7(c), illustrate that the predicted phase possesses lower free energy from 0 to approximately 907 K. Since its rate of decrease with temperature is more gradual than that of the observed phase, the free energy of the observed phase becomes lower when the temperature exceeds 907 K. This suggests that the predicted phase is more thermodynamically stable than the observed phase in the temperature range from 0 to 907 K, indicating that this predicted phase is very likely to be experimentally observable.

OPTICAL PROPERTIES

A material's optical behavior is characterized by several energy/frequency-dependent parameters, such as the dielectric function $\epsilon(\omega)$, absorption coefficient $\alpha(\omega)$, conductivity $\sigma(\omega)$, energy-loss function $L(\omega)$, reflectivity $R(\omega)$ and refractive index $n(\omega)$. The outcomes of these calculated properties are depicted in Fig. 8, based on formulas integrated within VASPKIT[19].

$$\epsilon(\omega) = \epsilon_1(\omega) + i\epsilon_2(\omega) \quad (13)$$

$$\alpha(\omega) = \frac{\sqrt{2}\omega}{c} \left[\sqrt{\epsilon_1^2 + \epsilon_2^2} - \epsilon_1 \right]^{\frac{1}{2}} \quad (14)$$

$$L(\omega) = \frac{\epsilon_2}{\epsilon_1^2 + \epsilon_2^2} \quad (15)$$

$$n(\omega) = \left[\frac{\sqrt{\epsilon_1^2 + \epsilon_2^2} + \epsilon_1}{2} \right]^{\frac{1}{2}} \quad (16)$$

$$R(\omega) = \frac{(n-1)^2 + k^2}{(n+1)^2 + k^2} \quad (17)$$

To examine the anisotropic characteristics, we calculated the optical parameters along the three principal axes and presented the optical spectra for incident photon energies up to 25 eV. For the predicted phase, these parameters are isotropic in the x- and y-directions. Therefore, Fig. 8 displays the optical parameters and the corresponding derived optical properties plotted only in the y- and z-directions for the predicted phase.

The complex dielectric function is essential for describing a material's optical properties, as it serves as the foundation from which other energy-dependent optical constants are derived. We illustrate the dielectric functions for both predicted and observed $\text{Na}_6\text{Ge}_2\text{Se}_6$ phases in Fig. 8(c) and (i), respectively. The real part of the dielectric function (ϵ_1) initially increases, reaches a peak, then sharply decreases, eventually dropping below zero. The imaginary part (ϵ_2), indicative of dielectric loss, closely aligns with the optical absorption coefficient. From the figure we can see ϵ_1 and ϵ_2 peak in different directions. For the predicted phase, ϵ_1 peaks in z-direction, and ϵ_2 peaks in y-direction. This contrasts with the observed phase, where both ϵ_1 and ϵ_2 peak in the same y-direction. The material's electronic characteristics can be inferred from the absorption coefficient ($\alpha(\omega)$), depicted in Fig. 8(a) and (g). Both phases begin to absorb at photon energies of approximately 3.1 eV and 2.9 eV respectively, indicating their optical band gaps. The absorption coefficients in three different directions follow a similar trend, with peaks at 7.4 eV for the predicted phase and 9.5 eV for the observed phase, both within the ultraviolet spectrum. The material's reflection and absorption properties, related to its loss function, are illustrated in Fig. 8(e)(k) and (d)(j). The edge trailing of the material's reflection and absorption spectra matches the peak in the loss function, showing a sharp increase around 12 eV for both phases. This spike indicates enhanced absorption and reflection of electromagnetic waves in the ultraviolet region, with the predicted phase exhibiting much notable anisotropy along y- and z-directions with the maximum appearing in y-direction for both phase. Optical conductivity which represents electrical conductivity over specific photon energy ranges is shown in Fig. 8(b) and (h). Conductivity sharply increases from zero at photon energies of 3.1 eV and 2.9 eV for the predicted and observed $\text{Na}_6\text{Ge}_2\text{Se}_6$ phases respectively, mirroring the optical band gap observed in the absorption curves in Fig. 8(a)(g). In summary, the predicted and observed phases display similar optical properties, with the predicted phase exhibiting a higher degree of optical anisotropy in the y- and z-directions, while being isotropic in the x- and y-directions.

CONCLUSION

A comprehensive comparison was conducted between two $\text{Na}_6\text{Ge}_2\text{Se}_6$ phases: a computationally predicted phase and an experimentally observed phase. This comparison spans their structural, elastic, electronic, phonon, thermal, and optical properties, employing first-principles methods.

The predicted $\text{Na}_6\text{Ge}_2\text{Se}_6$ phase is the energetically favored structure at zero pressure and temperature based on first-principles calculations. Both phases feature the identical $[\text{Ge}_2\text{Se}_6]$ dimer within their crystal structures, with significant differences observed in the bonding environment between Se and Na atoms (five Na atoms bond with one Se atom in the predicted phase, whereas six Na atoms bond with one Se atom in the observed phase).

Regarding elastic properties, both phases meet the criteria for mechanical stability and share similar characteristics. These include their resistance to volumetric and shape deformations, ductility, nature of bonding forces (central force), and bond bending as a major role in resisting external stress. The differences arise from their anisotropic characteristics. While the predicted phase is isotropic in the x- and y-directions, it exhibits greater anisotropy in the y- and z-directions compared to the observed phase.

Electronic structure analyses reveal a closely matched energy band gap between the two phases, primarily contributed by the $[\text{Ge}_2\text{Se}_6]$ dimers, with only a 1.3% difference. However, the electronic band structure indicates that the predicted phase exhibits an indirect band gap, while the observed phase has a direct band gap.

The optical behavior between the phases is similarly aligned, with both exhibiting a comparable optical band gap (3.1 eV for the predicted phase and 2.9 eV for the observed phase) and enhanced absorption and reflection of electromagnetic waves in the ultraviolet region. Although the predicted phase is isotropic in the x- and y-directions, it displays a greater degree of optical anisotropy in the y- and z-directions, aligning with the anisotropic nature identified in the elastic properties.

Phonon dispersion analyses affirm the dynamic stability of both phases. Further calculations of thermal properties indicate that the predicted phase is more thermodynamically stable in the temperature range from 0 to 907 K, suggesting a high likelihood of experimental observation.

ACKNOWLEDGEMENTS

The authors thank NSF, USA (grant No. DMR1809128) for the funding of this project. The authors also acknowledge the usage of the HPC cluster "Foundry" at Missouri S&T funded by NSF award OAC-1919789.

DATA AVAILABILITY STATEMENT

The data that support the findings of this study are available upon request.

-
- [1] N. Jia, M. Zhang, B. Li, C. Li, Y. Liu, Y. Zhang, T. Yu, Y. Liu, D. Cui, and X. Tao, *Electrochimica Acta* **320**, 134562 (2019).
- [2] J. Zhang, T. Li, B. Li, S. Zhang, Y. Dou, Q. Yuan, Y. Wu, and J. Han, *ACS Sustainable Chemistry & Engineering* **10**, 10666 (2022).
- [3] W.-C. Sun, S. U. Rahayu, and M.-W. Lee, *IEEE Journal of Photovoltaics* **8**, 1011 (2018).
- [4] H. Lin, G. Tan, J.-N. Shen, S. Hao, L.-M. Wu, N. Calta, C. Malliakas, S. Wang, C. Uher, C. Wolverton, *et al.*, *Angewandte Chemie International Edition* **55**, 11431 (2016).
- [5] Y. Pei, C. Chang, Z. Wang, M. Yin, M. Wu, G. Tan, H. Wu, Y. Chen, L. Zheng, S. Gong, *et al.*, *Journal of the American Chemical Society* **138**, 16364 (2016).
- [6] N. Ma, Y.-Y. Li, L. Chen, and L.-M. Wu, *Journal of the American Chemical Society* **142**, 5293 (2020).
- [7] N. Ma, F. Jia, L. Xiong, L. Chen, Y.-Y. Li, and L.-M. Wu, *Inorganic Chemistry* **58**, 1371 (2019).
- [8] S. Balijapelly, A. J. Craig, J. B. Cho, J. I. Jang, K. Ghosh, J. A. Aitken, A. V. Chernatynskiy, and A. Choudhury, *Journal of Alloys and Compounds* **900**, 163392 (2022).
- [9] P. F. Poudeu, J. D'Angelo, A. D. Downey, J. L. Short, T. P. Hogan, and M. G. Kanatzidis, *Angewandte Chemie International Edition* **45**, 3835 (2006).
- [10] A. K. Iyer, J. B. Cho, H. R. Byun, M. J. Waters, S. Hao, B. M. Oxley, V. Gopalan, C. Wolverton, J. M. Rondinelli, J. I. Jang, *et al.*, *Journal of the American Chemical Society* **143**, 18204 (2021).
- [11] A. C. Qi Zhang, Amitava Choudhury, submitted for publication to *J. Phys. Cond. Matter*. When it will be published we can update the citation..
- [12] B. Eisenmann, J. Hansa, *et al.*, *Materials research bulletin* **20**, 1339 (1985).
- [13] G. Kresse and J. Furthmüller, *Computational materials science* **6**, 15 (1996).
- [14] G. Kresse and J. Furthmüller, *Physical review B* **54**, 11169 (1996).
- [15] W. Kohn and L. J. Sham, *Physical review* **140**, A1133 (1965).
- [16] J. P. Perdew, K. Burke, and M. Ernzerhof, *Physical review letters* **77**, 3865 (1996).
- [17] A. V. Krukau, O. A. Vydrov, A. F. Izmaylov, and G. E. Scuseria, *The Journal of chemical physics* **125** (2006).
- [18] H. J. Monkhorst and J. D. Pack, *Physical review B* **13**, 5188 (1976).
- [19] V. Wang, N. Xu, J.-C. Liu, G. Tang, and W.-T. Geng, *Computer Physics Communications* **267**, 108033 (2021).
- [20] A. Togo, L. Chaput, T. Tadano, and I. Tanaka, *J. Phys. Condens. Matter* **35**, 353001 (2023).
- [21] A. Togo, *J. Phys. Soc. Jpn.* **92**, 012001 (2023).
- [22] S. P. Ong, W. D. Richards, A. Jain, G. Hautier, M. Kocher, S. Cholia, D. Gunter, V. L. Chevrier, K. A. Persson, and G. Ceder, *Computational Materials Science* **68**, 314 (2013).
- [23] S. Joergens and A. Mewis, *Zeitschrift für anorganische und allgemeine Chemie* **630**, 51 (2004).
- [24] K. Wu, Z. Yang, and S. Pan, *Inorganic Chemistry* **54**, 10108 (2015).
- [25] B. Eisenmann, E. Kieselbach, H. Schäfer, and H. Schrod, *Zeitschrift fuer Anorganische und Allgemeine Chemie* (1950) **516** (1984).
- [26] J. Schlirf and H. J. Deiseroth, *Zeitschrift für Kristallographie - New Crystal Structures* **216**, 27 (2001).
- [27] A. D. Becke and K. E. Edgecombe, *The Journal of chemical physics* **92**, 5397 (1990).
- [28] Y. Le Page and P. Saxe, *Physical Review B* **63**, 174103 (2001).
- [29] F. Mouhat and F.-X. Coudert, *Physical review B* **90**, 224104 (2014).
- [30] W. Voigt, *Lehrbuch der kristallphysik:(mit ausschluss der kristalloptik)*, Vol. 34 (BG Teubner, 1910).
- [31] A. Reuß, *ZAMM-Journal of Applied Mathematics and Mechanics/Zeitschrift für Angewandte Mathematik und Mechanik* **9**, 49 (1929).
- [32] S. Pugh, *The London, Edinburgh, and Dublin Philosophical Magazine and Journal of Science* **45**, 823 (1954).
- [33] C. Kittel and P. McEuen, *Introduction to solid state physics* (John Wiley & Sons, 2018).
- [34] A. T. Karim, M. Hadi, M. Alam, F. Parvin, S. Naqib, and A. Islam, *Journal of Physics and Chemistry of Solids* **117**, 139 (2018).
- [35] P. Ravindran, L. Fast, P. A. Korzhavyi, B. Johansson, J. Wills, and O. Eriksson, *Journal of Applied Physics* **84**, 4891 (1998).
- [36] O. L. Anderson and H. H. Demarest Jr, *Journal of Geophysical Research* **76**, 1349 (1971).
- [37] G. Vaitheeswaran, V. Kanchana, A. Svane, and A. Delin, *Journal of Physics: Condensed Matter* **19**, 326214 (2007).
- [38] L. Kleinman, *Physical Review* **128**, 2614 (1962).
- [39] J. Heyd, G. E. Scuseria, and M. Ernzerhof, *The Journal of chemical physics* **118**, 8207 (2003).
- [40] O. L. Anderson, *Journal of Physics and Chemistry of Solids* **24**, 909 (1963).
- [41] R. K. Fitzgerald and F. H. Verhoek, *The law of dulong and petit* (1960).
- [42] B. Fultz, *Progress in Materials Science* **55**, 247 (2010).
- [43] A. Togo and I. Tanaka, *Scripta Materialia* **108**, 1 (2015).